nature photonics

SUPPLEMENTARY INFORMATION

DOI: 10.1038/NPHOTON.2015.196

Optical control of excitation waves in cardiac tissue

Burton RAB, Klimas A, Ambrosi CM, Tomek J, Corbett A, Entcheva E, Bub G

Image processing: In some cases, excitation waves are visible without image processing (**Supplementary Movie 2**). Visibility of excitation waves was enhanced during live recording by applying a running background subtraction followed by an absolute value operation on each pixel:

$$p_t(i,j) = |p_t(i,j) - p_{t-n}(i,j)| \qquad \textit{eq. S1}$$

Where $p_t(i,j)$ is the value of pixel p at location i,j at time t, and $p_{t-n}(i,j)$ is the value of the same pixel at an earlier time point (typically 120ms, or 6 frames apart). The low computational overhead of this filter operation allowed assessment of activity in real time.

An example of the output of this operation are the two frames in **Fig 1b**. Plotting the filtered intensity vs. time curves for the data yields a doubled humped curve, where the first spike corresponds to activation and the second hump corresponds to relaxation (**Supplementary Figure 1**). Data filtered in this fashion can be directly used for analysing simple wave dynamics (e.g. calculation of conduction velocity for planar waves). However, interpretation of complex spiral and wavelet patterns were hindered by the presence of the second hump, as it was often difficult to distinguish excitation from relaxation waves. We employed a different method to measure the shape of excitation waves (see below) for generating the activation maps in the paper.

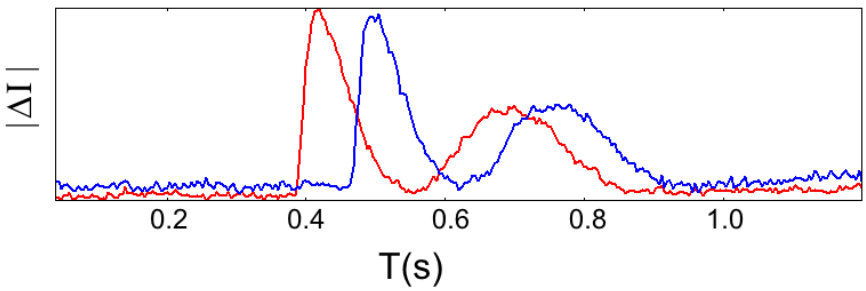

Supplementary Figure 1: Characteristic double humped curve following application of the absolute difference filter (Eq S1), for two locations in the path of a travelling wave front.

Measurement of activation wave patterns (**Fig 1d, 4c**, main text) was achieved as follows. After acquisition, a running background subtraction (where each pixel at frame ***t*** is replaced by its value minus the average value of that pixel between ***t-n*** and ***t+n***) gives a clear image of wave dynamics (**Supplementary Movie 1** and **Supplementary Movie 3**). The dichroic mirror and band pass filters pass a small amount of excitation light so that the imposed illumination patterns are directly visible in this record.

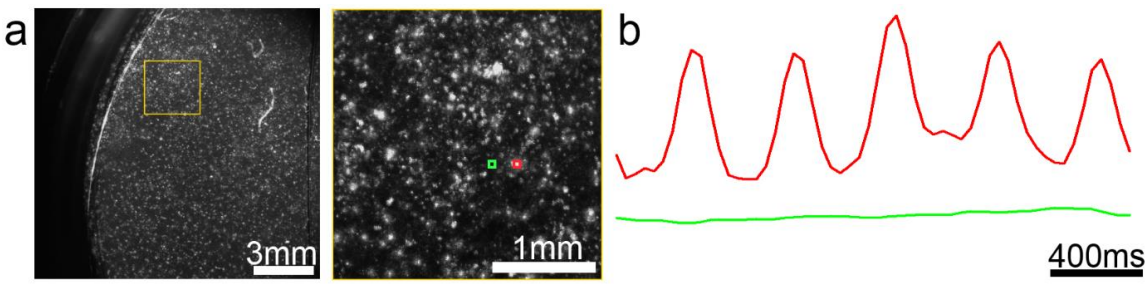

Supplementary Figure 2: Raw data consists of high contrast regions distributed throughout the sample. A) Full field of view single frame. The edge of the 35mm petri dish is clearly visible. The second panel in is a full resolution zoom showing bright and dark regions. B) Intensity vs. time plots from pixels in panel 'a' show markedly different transients. Bright regions (red ROI in 'a') in the image are more likely to show activity related to contraction of the monolayer than dark regions (green box in 'a').

DOI: 10.1038/NPHOTON.2015.196

Quantification of wavefront location was performed in several steps. Off-axis illumination results in localised regions of high contrast (**Supplementary Figure 2a**). We find that these regions typically display an increase in intensity that corresponds to contraction, while darker regions do not display transients that can be distinguished from noise (**Supplementary Figure 2b**). The data sets generated from our imaging technique yield a sparse set of points that we use to track the continuous contraction waves in the underlying tissue.

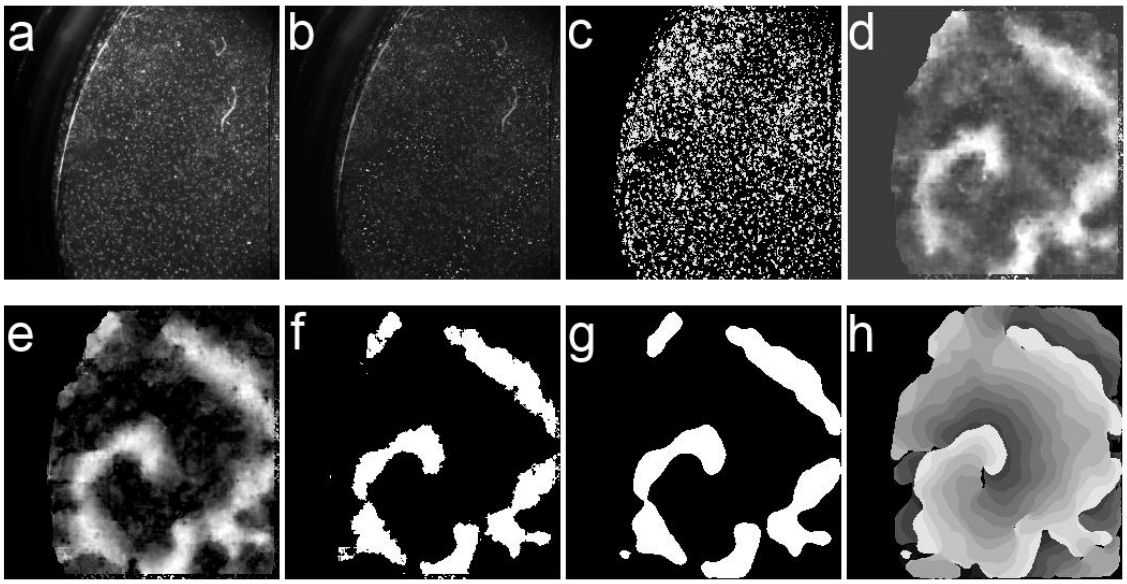

Supplementary Figure 3: Data analysis steps. A) Raw data. B) A running background subtraction operation can reveal waves if images are played back sequentially. C) A threshold operation finds bright areas in the image, these are used to generate a mask as shown. D) The pixels found in 'c' are used to reconstruct the wavefront. E) Cross correlation with a single transient removes noise; F) a thresholding operation followed by dilation/erosion (panel G) gives the final wave location. H) The waves are used to construct isochronal maps as described in the text.

We first spatially bin images by a factor of 8 prior to processing in order to reduce computation time. The data is then scaled between 0 and 1, and all pixels with average value less than 0.1 are classified as nonresponsive and all pixels with average value equal or greater than 0.1 are classified as responsive (**Supplementary Figure 3c**). Nonresponsive pixels are replaced by the average of those responsive pixels within a radius of 8 (binned) pixels for each frame. After this operation, responsive pixels are also spatially averaged (radius 8) (**Supplementary Figure 3d**). Intensity as a function of time traces for each pixel are then cross correlated against a single transient from a representative active pixel. The value of the cross correlation is then used to generate a data set that is used to locate wavefronts (**Supplementary Figure 3e**). Isochronal maps, which show the location of the wave front over several frames (**Supplementary Figure 3h**), are generated by performing a threshold operation (pixel intensity>50% maximum) on the cross correlation data sets (**Supplementary Figure 3f**) and replacing the active pixels with a time stamp. Sequential frames are collapsed into one frame so that time of activation values overwrite existing values if the difference between them is greater than 50 ms (the minimum refractory period) (**Supplementary Figure 3h**). Isochronal lines are found using a marching squares algorithm, and colour coded using the 'rainbow smooth.lut' lookup table from ImageJ.

Validation and characterisation of the dye-free imaging - comparison with voltage sensitive dye records (Supplementary Figure 4): In control experiments, we used a voltage-sensitive fluorescent dye to confirm that the dye-free imaging modality mapped cardiac excitation. Cardiac monolayers were stained with the membrane potential dye FluoVolt (Molecular Probes/Life technologies). The loading solution consisted of 100 μL PowerLoad (Molecular Probes/Life technologies) 100X concentrate and 10 μL FluoVolt dye at 1000X, mixed (by vortex) in a 15mL tube; 10mL of Hank's balanced salt solution (HBSS) was added and mixed well. The cell culture medium was gently removed from the plates and cells were washed twice in PBS. 2mL of FluoVolt loading solution was added to the monolayer and the cells were incubated at room temperature for 30 minutes. FluoVolt loading solution was gently removed and the cells washed three times with PBS. 2mL of HBSS was added to the plates for live-cell imaging using a Photometrics Evolve 128 EMCCD camera binned to 32x32 pixels.

We performed imaging of membrane voltage using a fluorescent voltage sensitive dye (Fluovolt) through a 10x objective at 620 frames/second while simultaneously capturing waves by the dye-free method with a 1x objective at 100 frames/second. Acquisition start time was synchronised via TTL to allow temporal registration of the signals (**Supplementary Figure 4**). The ability to simultaneously capture images from both sides of the preparation is a second differentiating feature of the dye-free imaging modality presented here in comparison to the method by Lee's group[5,6] since the illumination path is oblique to the primary optical axis, we are able to acquire images on both sides of the preparation with two independent objectives.

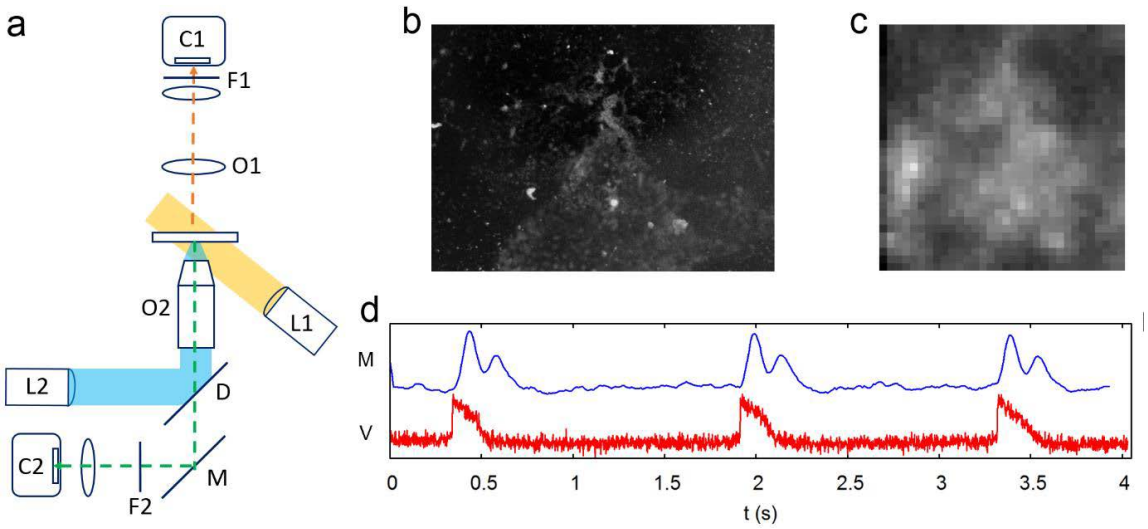

Supplementary Figure 4: simultaneous dye-free and voltage dye mapping of cardiac monolayer cultures is used to validate the new imaging modality for tracking excitation wavefronts. **a)** Diagram of the imaging setup (L1 white LED with orange filter; L2 blue LED; O1 1x objective, Olympus MVX10; O2 10x objective (Nikon); F1 bandpass filter (580±20nm); F2 bandpass filter (535±20nm); D dichroic at 505nm; C1 Andor Neo sCMOS camera, 100 f/s; C2 Photometrics Evolve EMCCD 128, 620 f/s); **b)** A macroscopic image of the monolayer captured using the sCMOS camera; **c)** A microscopic image captured with the high speed Evolve EMCCD; **d)** Intensity vs time plots for the dye-free transients (blue, obtained from pixels in the blue square in panel b, after filtering as described in **Supplementary Figure 3**) and membrane voltage (red, obtained from pixels in the red square in panel c). The cameras were aligned before imaging so that the red square and blue square cover the same location.

DOI: 10.1038/NPHOTON.2015.196

Validation and characterisation of the dye-free imaging – coherence effects (Supplementary Figure 5):

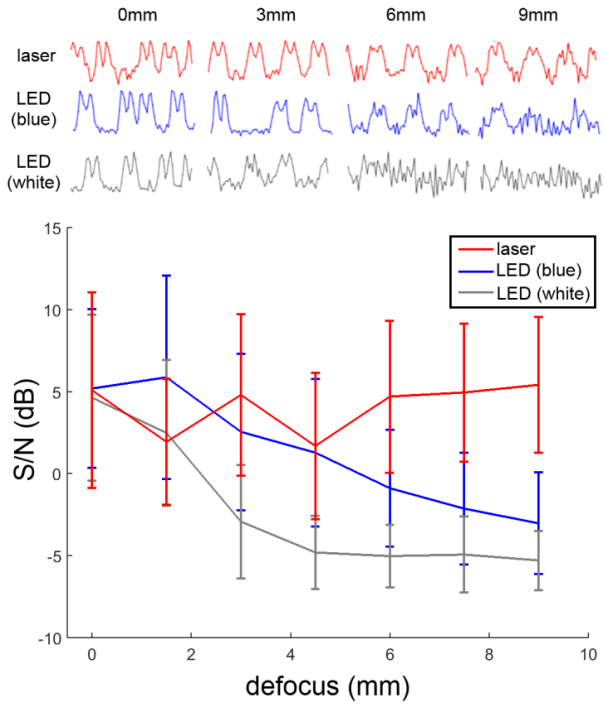

Supplementary Figure 5: Comparison of the performance of three light sources as a function of distance from the focal plane (defocus). A red diode laser, blue LED and white LED were used while imaging a cardiac monolayer at 6 positions of defocus. Image sequence S/N was calculated by dividing the field of view into 64 square grid, extracting time series from each grid location (Figure S1, top panel), applying Eq. S1, calculating the S/N for each trace and averaging these to obtain the mean value. Error bars are the standard deviation for the 64 traces.

We experimentally characterised the performance of the imaging system using three light sources which differ in their spatial and temporal coherence: a white LED, a blue LED (Cairn Research), and a red laser (Thorlabs CPS186), imaging spontaneously active samples (**Supplementary Figure 5**). The three light sources were held within the same optical mount, and a series of images were captured at different focal planes (every 1.25mm) using a mechanical focus motor (Prior Scientific H22) to move the objective to ensure that the image series can be directly compared. The image contrast was assessed for the three light sources by measuring the signal to noise ratio (Matlab 'snr' function) of time-varying intensity (raw image data was first filtered using Eq. S1, described above), extracted from 64 equidistant regions of interest within 200 frame image sequences. Light sources were adjusted so that waves were visible at the focal plane. When in perfect focus, all three sources can image wave activity and show strong spikes in the intensity vs time plots (SNR>5 decibels). When defocused, the white LED loses signal rapidly, while the more coherent blue LED maintains signal over several millimetres. The difference in signal quality is significant for the LED sources ($P<0.01$, t-test and Wilcoxon ranksum) for all defocus values over 0. The laser, with the highest coherence, maintains a high SNR over the entire defocus range. This dependence of image quality on the spectral bandwidth (coherence) of the light source is indicative of likely interference contribution to the image formation. The modulation of the phase profile of the source by the excitation-contraction wave produces localised changes in the detected interference pattern, which can be isolated by temporally filtering the image (see **Image Processing**, Eq. S1).

To our knowledge, the dye-free imaging reported here is a novel method for tracking *macroscopic cardiac wave dynamics*, following one different implementation by Lee and colleagues[1,2], who used a transport-of-intensity equation[3] to explain their method. In contrast to their system, our approach allows for capture of wave dynamics even when the sample is defocused (Supplementary Fig. 5), which is advantageous in long-term observations or when imaging multiple samples (e.g. high throughput screening applications). We note that dye-free (or intrinsic) imaging has been used in excitable neural (and some muscle) preparations for over 40 years employing a variety of different albeit related methods[4–12]. In the available literature, there is still little consensus on a dominant contrast mechanism in dye-free imaging, where interferometric, scattering and birefringence contributions have been discussed (e.g. see references 11 and 14 below). Image formation in the implementation, introduced in this Letter, is likely the result of the combined effects of interference (see **Supplementary Figure 5**) and other contrast enhancing effects (e.g. scattering).

The dye-free imaging methods used here (as well as the method used by Lee et al[1,2]) function by allowing dynamic microscopic (cell-level) changes in optical properties due to excitation-contraction events to be visualised macroscopically. These dye-free signals provide a surrogate for membrane voltage (action potentials), and as such, they have certain limitations. For example, the dye-free signals lack the sharp upstroke of the action potential waveform, which may increase uncertainty when extracting times of activation and measuring conduction velocity[13]. In addition, the dye free method will be less reliable in characterising conduction in pathological cases, where excitation-contraction coupling is compromised[14]. However, in most experimental contexts, cellular contraction follows excitation at a set interval[15,16], and dye-free imaging provides an accurate representation of conduction velocity, wave dynamics and pattern formation. Indeed, calcium transients are often used as a surrogate for membrane voltage in cardiac monolayer experiments[17], and contraction is tightly linked to cytoplasmic calcium concentrations.

Camera and DMD Control: The camera and DMD were controlled using custom written Java based software. Java JNI (Java Native Interface) wrappers were written to access Andor (for the Neo sCMOS camera) and Vialux (for the DMD) C based SDKs. Software for displaying the camera in real time, storing and analysing the data, and controlling the DMD is written in a combination of Java and Python, and is available directly from the authors.

Sequences of binary images were downloaded to the Vialux DMD unit and projected onto the sample. Precise control of the light level is achieved by controlling the LED current and by simulating grey levels by rapidly toggling the DMD state. For example, the fine steps in light level for **Fig 3d** were achieved by projecting patterned light every 5th frame with a duty cycle of 500 μs, and increasing LED current between 0 and 25% maximum intensity.

Sequences of spiral wave patterns were generated by simulating clockwise and counter-clockwise rotating spiral waves in a cellular automaton excitable media (CA) model. Details of the CA can be found in reference 31 (main text online methods). A CA with dimensions 256x192 (one quarter of the DMDs XGA resolution), with neighbourhood size 20, A (active) time of 3 and R (refractory) time of 7 was initialised with a wavefront extending over half the field and iterated with a threshold of 0.24. The simulation was iterated 40 times to obtain a stable spiral shape. The CA was iterated and individual frames were uploaded to the DMD using the following steps. First, the image was upscaled to 1024x768 pixels using nearest neighbour interpolation. Two frames were then uploaded to the DMD for each CA iteration, where frame 1 contained all active and refractory cells, and frame 2 contained only refractory cells. Repeating these steps 40 times results in 80 frames uploaded to the DMD, where the activation wavefront is half the intensity of the refractory wavefront. The rotation speed of the projected spiral is controlled by varying the time between projected frames.

Measurement of conduction velocity: Conduction velocity is determined by measuring the activity in two locations that are separated by a distance ***d*** in the path of a travelling wave. Raw data is temporally processed (Eq. S1), intensity vs. time plots from these two locations are scaled between 0

DOI: 10.1038/NPHOTON.2015.196

and 1, and the time of activation is determined for each waveform from when the waveform crosses 0.5. The conduction velocity is calculated from the differences in the two time measures and the distance between the measuring sites.

We observe a linear relationship between light intensity and conduction velocity in optogenetically modified monolayers in 9 experiments. We fit a regression line to the measured velocities and then calculate the $\mathbf{r^2}$ goodness of fit statistic as well as the standard error of regression (**S**). The p value of the F-test is used to assess whether the measured slope is significantly non-zero. In all but one experiment we find a good linear fit ($p<0.01$) to the data. The residuals compared to a linear fit for all experiments are shown in Supplementary Figure **6b**.

The variations in the slope of the curves are likely due to natural variability between samples and inter-experiment variation in viral delivery and expression. It should be noted that optically-mediated increase in CV is demonstrated here in poorly-coupled cardiac networks (CV < 40 mm/s); well coupled cardiac tissue may have limited capacity to augment CV by optogenetic stimulation.

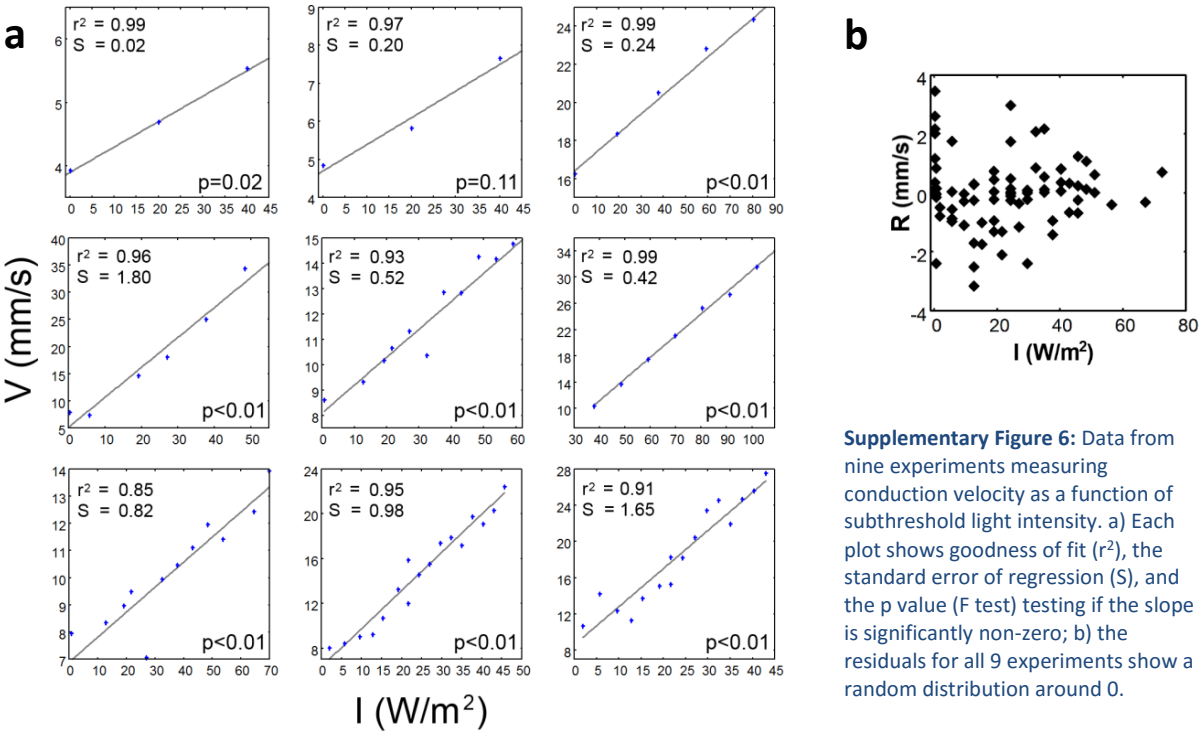

Supplementary Figure 6: Data from nine experiments measuring conduction velocity as a function of subthreshold light intensity. a) Each plot shows goodness of fit (r^2), the standard error of regression (S), and the p value (F test) testing if the slope is significantly non-zero; b) the residuals for all 9 experiments show a random distribution around 0.

Measurement of chirality reversal: Chirality reversal was achieved by overwriting an existing spiral by a moving image of a counter-rotating spiral generated by a cellular automaton model (see **Camera and DMD control**, above). Experiments were carried out by first locating a spiral core in the sample and roughly aligning the spiral core with the centre of the field of view. All experimental runs were successful when the imposed spiral core was closely aligned with the existing spiral (**Fig 4**, **Supplementary Movie 4 and 5**). However the cardiac monolayer preparation we use in these experiments displayed spontaneous activity and each monolayer could potentially support multiple interacting spiral centres that meander and change positions over time. There was a time delay of several minutes between locating a spiral core and projecting the imposed spiral, at which point in some experiments the original spiral core would no longer be located near the centre of the imaging field of view. Experiments where a spiral is imposed on an off-centre existing spiral result in two spiral waves (the newly created spiral and the pre-existing spiral) but no change in chirality. **Supplementary Movie 6** shows minimally processed data (filtered with Eq. S1) of several chirality reversal experiments.

Manipulation of excitable waves at macroscopic (>5mm^2) space scales		
method	**advantages & unique features**	**disadvantages**
Electrical (extracellular multielectrode) [18,19]	• Simple & minimally invasive • High temporal resolution • Routinely used in vivo, long-term	• Limited spatial resolution/targeting (far field effects limit resolution) hence unsuitable for wave control • Cannot be cell type-specific • Long clamp pulses are not feasible due to Faradaic effects
Chemical [20–22]	• Simple, applicable in vivo • Spatially localisable (via uncaging) • Cell-specific due to receptor specificity	• Lacks temporal resolution, hence unsuitable for dynamic wave control • Uncaging cannot be applied repeatedly
Optical (non-optogenetic: thermal and others) [23–29]	• Applicable in vivo without genetic manipulations • Applicable long-term • High temporal and spatial resolution for triggering activation • Better depth penetration due to longer wavelengths used	• Cannot be cell type-specific • Cannot provide bi-directional voltage control (depolarisation/hyperpolarisation) • Long time and/or space clamps are not feasible (sharp temperature gradients in space/time are essential for its operation) • Mechanism of action not well understood
Optogenetic (e.g. refs [30,31] and Figures 1-4 in this paper)	• Ability to clamp voltage in time and space, operation at low irradiance • Permits cell-specific targeting • Permits bi-directional control (depolarisation and hyperpolarisation) • Well tolerated for long-term studies	• Need to genetically modify tissue • Depth actuation in vivo problematic
Sensing/imaging of excitable waves at macroscopic (>5mm^2) space scales		
Electrical (multielectrode) [19,32,33]	• Non-invasive • High temporal resolution • Suitable for measuring conduction	• Very limited spatial resolution (orders of magnitude poorer than optical methods) • Depth imaging in vivo problematic
Optical (fluorescent probes) imaging[34,35]	• High spatiotemporal resolution • Provides information about electrophysiological characteristics, e.g. action potentials and calcium transients, in addition to conduction	• Not suitable for long-term monitoring due to phototoxicity • Bulky/sophisticated detectors and optics, not amenable to miniaturisation • Depth imaging in vivo problematic
Optogenetic (fluorescence) imaging[36,37]	• Possible long-term in vivo imaging • Cell-specific reporting possible • Provides added information about electrophysiological characteristics, e.g. action potentials and calcium transients	• Need to genetically modify tissue • Bulky/sophisticated detectors and optics, not amenable to miniaturisation; • Depth imaging in vivo problematic
Dye-free imaging (methodology in refs [1,2] and Fig 1 in this paper)	• Simple and most cost-effective • Spectrally-flexible • Non-invasive (good for long term study) • High spatiotemporal resolution • Easily miniaturised	• Tissue imaging in vivo needs alternative implementation • Depth imaging in vivo problematic • Only indirect measure of important electrophysiological characteristics (e.g. action potential shape)

Supplementary Table 1: Comparison of methods for manipulation and sensing of excitation waves at macroscopic resolutions. An ideal methodology for manipulating excitation waves at the tissue level requires rapid, multi-site stimulation over macroscopic fields of view. Similarly, an ideal imaging modality allows determination of activation wave morphology without damaging the tissue. The references included in the table do not only highlight papers where macroscopic manipulation and/or imaging of wavefronts is achieved, but may give examples of the techniques operating at microscopic space scales (e.g. optical/thermal actuation) for comparison purposes.

DOI: 10.1038/NPHOTON.2015.196

Supplementary References:

1. Hwang, S., Yea, K. & Lee, K. J. Regular and alternant spiral waves of contractile motion on rat ventricle cell cultures. *Phys. Rev. Lett.* **92,** 198103 (2004).

2. Hwang, S.-M., Kim, T. Y. & Lee, K. J. Complex-periodic spiral waves in confluent cardiac cell cultures induced by localized inhomogeneities. *Proc. Natl. Acad. Sci. U. S. A.* **102,** 10363–10368 (2005).

3. Barty, A., Nugent, K. A., Paganin, D. & Roberts, A. Quantitative optical phase microscopy. *Opt. Lett.* **23,** 817 (1998).

4. Cohen, L. B., Keynes, R. D. & Hille, B. Light Scattering and Birefringence Changes during Nerve Activity. *Nature* **218,** 438–441 (1968).

5. Cohen, L. B., Keynes, R. D. & Landowne, D. Changes in axon light scattering that accompany the action potential: current-dependent components. *J. Physiol.* **224,** 727–52 (1972).

6. He, H. *et al.* Application of sphere-cylinder scattering model to skeletal muscle. *Opt. Express* **18,** 15104–12 (2010).

7. Stepnoski, R. A. *et al.* Noninvasive detection of changes in membrane potential in cultured neurons by light scattering. *Proc. Natl. Acad. Sci.* **88,** 9382–9386 (1991).

8. Shaked, N. T., Satterwhite, L. L., Bursac, N. & Wax, A. Whole-cell-analysis of live cardiomyocytes using wide-field interferometric phase microscopy. *Biomed. Opt. Express* **1,** 706–719 (2010).

9. Katz, G. M., Mozo, A. & Reuben, J. P. Filament interaction in intact muscle fibers monitored by light scattering. *Proc. Natl. Acad. Sci. U. S. A.* **76,** 4421–4 (1979).

10. Xia, J., Weaver, A., Gerrard, D. E. & Yao, G. Monitoring sarcomere structure changes in whole muscle using diffuse light reflectance. *J. Biomed. Opt.* **11,** 040504

11. Baylor, S. M. & Oetliker, H. A large birefringence signal preceding contraction in single twitch fibres of the frog. *J. Physiol.* **264,** 141–62 (1977).

12. Grinvald, A., Lieke, E., Frostig, R. D., Gilbert, C. D. & Wiesel, T. N. Functional architecture of cortex revealed by optical imaging of intrinsic signals. *Nature* **324,** 361–4

13. Laughner, J. I., Ng, F. S., Sulkin, M. S., Arthur, R. M. & Efimov, I. R. Processing and analysis of cardiac optical mapping data obtained with potentiometric dyes. *AJP Hear. Circ. Physiol.* **303,** H753–H765 (2012).

14. Ren, J. & Bode, A. M. Altered cardiac excitation-contraction coupling in ventricular myocytes from spontaneously diabetic BB rats. *Am. J. Physiol. Heart Circ. Physiol.* **279,** H238–44 (2000).

15. Bers, D. M. Calcium Fluxes Involved in Control of Cardiac Myocyte Contraction. *Circ. Res.* **87,** 275–281 (2000).

16. Peeters, G. A., Hlady, V., Bridge, J. H. & Barry, W. H. Simultaneous measurement of calcium transients and motion in cultured heart cells. *Am J Physiol Hear. Circ Physiol* **253,** H1400–1408 (1987).

17. Bub, G. Bursting calcium rotors in cultured cardiac myocyte monolayers. *Proc. Natl. Acad. Sci.* **95,** 10283–10287 (1998).

18. Spira, M. E. & Hai, A. Multi-electrode array technologies for neuroscience and cardiology. *Nat. Nanotechnol.* **8,** 83–94 (2013).

19. Xu, L. *et al.* 3D multifunctional integumentary membranes for spatiotemporal cardiac measurements and stimulation across the entire epicardium. *Nat. Commun.* **5,** 3329 (2014).

20. Lee, P. *et al.* Simultaneous measurement and modulation of multiple physiological parameters in the isolated heart using optical techniques. *Pflugers Arch.* **464,** 403–14 (2012).

21. Arutunyan, A., Webster, D. R., Swift, L. M. & Sarvazyan, N. Localized injury in cardiomyocyte network: a new experimental model of ischemia-reperfusion arrhythmias. *Am. J. Physiol. Heart Circ. Physiol.* **280,** H1905–H1915 (2001).

22. Lin, J. W. *et al.* Region [corrected] of slowed conduction acts as core for spiral wave reentry in cardiac cell monolayers. *Am. J. Physiol. Heart Circ. Physiol.* **294,** H58–65 (2008).

23. Jenkins, M. W. *et al.* Optical pacing of the embryonic heart. *Nat. Photonics* **4,** 623–626 (2010).

24. Jenkins, M. W. *et al.* Optical pacing of the adult rabbit heart. *Biomed. Opt. Express* **4,** 1626–35 (2013).

25. Izzo, A. D., Richter, C.-P., Jansen, E. D. & Walsh, J. T. Laser stimulation of the auditory nerve. *Lasers Surg. Med.* **38,** 745–53 (2006).

26. Dittami, G. M., Rajguru, S. M., Lasher, R. A., Hitchcock, R. W. & Rabbitt, R. D. Intracellular calcium transients evoked by pulsed infrared radiation in neonatal cardiomyocytes. *J. Physiol.* **589,** 1295–1306 (2011).

27. Shapiro, M. G., Homma, K., Villarreal, S., Richter, C.-P. & Bezanilla, F. Infrared light excites cells by changing their electrical capacitance. *Nat. Commun.* **3,** 736 (2012).

28. Wells, J. *et al.* Optical stimulation of neural tissue in vivo. *Opt. Lett.* **30,** 504–6 (2005).

29. Smith, N. I. *et al.* A femtosecond laser pacemaker for heart muscle cells. *Opt. Express* **16,** 8604 (2008).

30. Bruegmann, T. *et al.* Optogenetic control of heart muscle in vitro and in vivo. *Nat. Methods* **7,** 897–900 (2010).

31. Jia, Z. *et al.* Stimulating Cardiac Muscle by Light Cardiac Optogenetics by Cell Delivery. *Circ. Arrhythmia Electrophysiol.* **4,** 753–760 (2011).

32. Narayan, S. M. *et al.* Treatment of atrial fibrillation by the ablation of localized sources: CONFIRM (Conventional Ablation for Atrial Fibrillation With or Without Focal Impulse and Rotor Modulation) trial. *J. Am. Coll. Cardiol.* **60,** 628–36 (2012).

33. Triedman, J. K. *et al.* Multipolar endocardial mapping of the right heart using a basket catheter: acute and chronic animal studies. *Pacing Clin. Electrophysiol.* **20,** 51–9 (1997).

34. Efimov, I., Nikolski, V. & Salama, G. Optical imaging of the heart. *Circ. Res.* **95,** 21–33 (2004).

35. Tung, L. & Zhang, Y. Optical imaging of arrhythmias in tissue culture. *J. Electrocardiol.* **39,** S2–6 (2006).

36. Knöpfel, T. Genetically encoded optical indicators for the analysis of neuronal circuits. *Nat. Rev. Neurosci.* **13,** 687–700 (2012).

37. Kralj, J. M., Douglass, A. D., Hochbaum, D. R., Maclaurin, D. & Cohen, A. E. Optical recording of action potentials in mammalian neurons using a microbial rhodopsin. *Nat. Methods* **9,** 90–5 (2012).

DOI: 10.1038/NPHOTON.2015.196

SUPPLEMENTARY MOVIES

Supplementary Movie 1: Raw data of wave activity in the monolayer preparation imaged using the dye free system described in **Fig 1**. The first three seconds show the entire field of view (2064 by 2048 pixels or 13.4 by 13.3 mm). The last three seconds show a 400 x 400 pixel zoom at full resolution (1:1). Scale bars are shown in **Supplementary Figure 2**. Travelling waves are visible at both resolutions.

Supplementary Movie 2: Demonstration of conventional optogenetic actuation of wave activity in a monolayer preparation. Right side (a) shows minimally processed data (running background subtraction operation), the left side (b) shows processed images (see **Supplementary Figure 2** and accompanying text). A strong light pulse (maximum intensity) removes an existing spiral. The tissue is subsequently placed with a rectangular wave form to generate planar waves. Spontaneous activity (originating outside the field of view) commences once pacing is stopped. Isochronal maps of the activity before and during pacing is shown in **Fig 1d**.

Supplementary Movie 3: Conduction velocity modulation of a travelling wave using different sub threshold intensity light. The first part of the movie shows velocity increase in the leftward direction for three different intensities (a: no light; b: 20 W/m^2; c: 40 W/m^2), and the second part shows velocity increase in the rightward direction for the same preparation.

Supplementary Movie 4: Chirality change in a spiral using an optically imposed spiral rotating in the opposite direction. Chirality change is achieved four times. The data is minimally processed (running average background subtraction over 20 frames), allowing visualisation of wave patterns as well as the applied optical stimulus. The movie plays back in real time.

Supplementary Movie 5: Processed and colourised version of Movie 4. The data is processed to step 'd' in Figure S2 to accentuate wave fronts, and a colour map is applied so that waves show in green and imposed excitation patterns show in red.

Supplementary Movie 6: Additional minimally processed data sets demonstrating chirality reversal, here using a running background subtraction followed by an absolute value operation on each pixel. Each example is preceded by a title slide giving an explanation of the observed dynamics.